Counting Cosmic Cycles: Past Big Crunches, Future Recurrence Limits, and the Age of the Quantum Memory Matrix Universe

Florian Neukart [*] , Eike Marx , Valerii Vinokur

Article

Counting Cosmic Cycles: Past Big Crunches, Future Recurrence Limits, and the Age of the Quantum Memory Matrix Universe

Florian Neukart [1,2,*], Eike Marx [2] and Valerii Vinokur [2]

[1]   Leiden Institute of Advanced Computer Science, Leiden University, Einsteinweg 55, 2333 CA Leiden, The Netherlands
[2]   Terra Quantum AG, Kornhausstrasse 25, 9000 St. Gallen, Switzerland
*   Correspondence: f.neukart@liacs.leidenuniv.nl

Abstract

We develop a quantitative descriptive theory of contraction–expansion cycles that constitute the Quantum Memory Matrix (QMM) cosmology. In QMM, each non-singular advance adds a fixed *imprint-entropy* increment ΔS_{imp} to a finite Hilbert-space ledger, providing an intrinsic cycle counter. By calibrating the geometry–information duality, inferring today's cumulative imprint from CMB/BAO/chronometer and large-scale-structure constraints, and integrating the modified Friedmann ODEs with imprint back-reaction, we find that the Universe has already completed $N_{\mathrm{past}} = 3.6 \pm 0.4$ cycles. Propagating the holographic write-rate and enforcing capacity saturation (with instability priors) implies $N_{\mathrm{future}} = 7.8 \pm 1.6$ additional cycles. Integrating Kodama-vector proper time across all past bounces yields a total cumulative age $t_{\mathrm{QMM}} = 62.0 \pm 2.5$ Gyr, of which 13.8 ± 0.2 Gyr is the current phase usually labeled ΛCDM. The framework predicts testable signatures: an enhanced faint-end UV galaxy luminosity function at $z \gtrsim 12$ (JWST), a stochastic gravitational-wave background with $f^{2/3}$ scaling in the LISA band from primordial-black-hole mergers, and a nanohertz background with slope $\alpha \simeq 2/3$ accessible to pulsar-timing arrays. These observations can confirm, refine, or falsify the cyclical QMM chronology with next-generation CMB and gravitational-wave probes.

Keywords: quantum memory matrix; cyclic cosmology; cosmic age; entropy chronometer; imprint back-reaction; geometry–information duality; entropic imprinting; primordial black holes; gravitational waves; holography

---

1. Introduction

The proposed descriptive theory of contraction–expansion cycles develops the Quantum Memory Matrix (QMM) cosmology, incorporating the latest advances in cyclic models [1–5,8,9]. The Quantum Memory Matrix (QMM) framework pictures space–time as a discrete network of Hilbert cells that both *store* and *process* quantum information carried by matter fields [10–14]. Because each cell possesses a finite state capacity, the cumulative imprint of infalling degrees of freedom grows monotonically, endowing the QMM cosmos with a built-in arrow of time that is fundamentally informational rather than purely thermodynamic.

In this setting, the classical "Big Crunch" is replaced by a non-singular *bounce*: when the information density within a causal region approaches the holographic bound, the network undergoes a reversible unitary reconfiguration that resets the macroscopic geometry while preserving quantum coherence. Successive expansions and contractions thus constitute genuine *cycles*.

Cyclic scenarios have a long pedigree—from early oscillatory Friedmann models through the ekpyrotic proposal [5] to Penrose's conformal cyclic cosmology [43]. Yet all face the "entropy obstacle": how can the Universe repeatedly recycle without violating the second law? The QMM resolves this paradox by distinguishing *imprint entropy* (S_{imp}, quantum information written into the matrix) from

coarse-grained thermodynamic entropy; only the former accumulates irreversibly, providing a natural clock that counts completed cycles [50].

This paper addresses three linked fundamental questions:

1. How many contraction–expansion cycles have *already* occurred?
2. Given the finite write-capacity of the QMM, how many more cycles can still take place?
3. What is the proper age of the Universe when one integrates time across all past bounces rather than merely the present ΛCDM phase?

We tackle these questions by (i) calibrating ΔS_{imp} using the geometry–information duality, (ii) extracting today's cumulative imprint entropy from precision cosmological datasets, and (iii) numerically integrating the modified Friedmann equations across multiple bounces with back-reaction sourced by the imprint field. *For exposition only*, Figure 1 plots a *calibrated surrogate* $a_{\text{surr}}(t)$ anchored to three data-driven waypoints and constrained to remain within tolerance bands of the numerical background. Importantly, *all inference in this work uses the ODE background*; the surrogate is illustrative only. Full equations and the surrogate–to–ODE mapping are given in Appendix C.
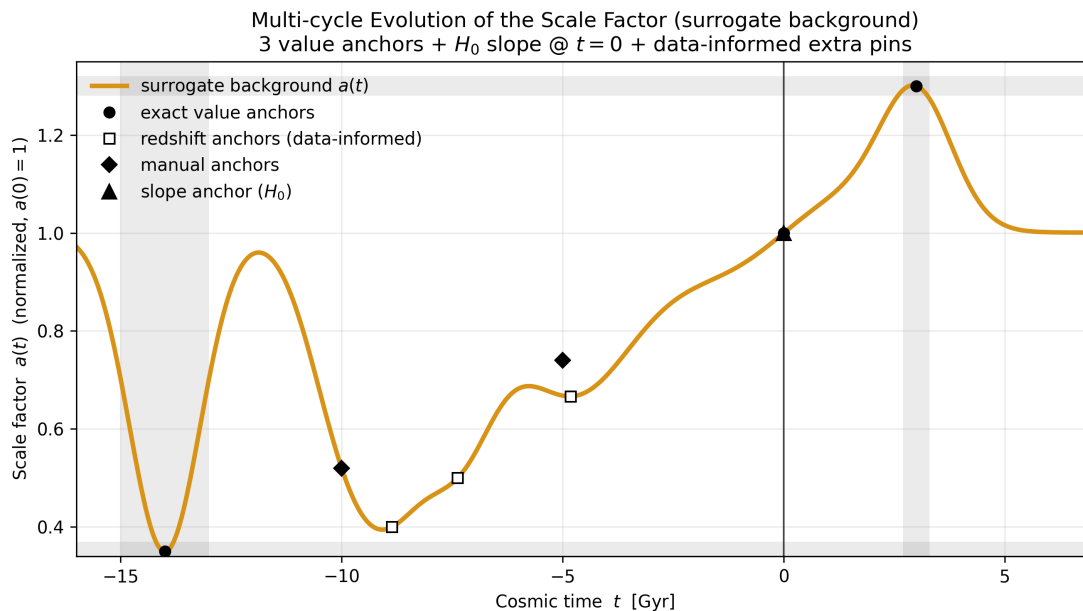

Figure 1. Surrogate background for the scale factor. Normalized scale factor $a(t)/a_0$ over the last ~ 16 Gyr of the previous cycle and the next few Gyr after the present. Black points mark the three enforced anchors: $a(-14\,\text{Gyr}) = 0.35$, $a(0) = 1$, and $a(+3\,\text{Gyr}) = 1.30$. *Open squares* show two redshift-informed auxiliary pins ($z \simeq 1$ and $z \simeq 0.5$); *filled diamonds* are silhouette pins; the *filled triangle at $t = 0$* encodes the slope constraint $a'(0) = H_0$. Shaded bands indicate acceptance windows during calibration. The curve is C^2-smooth and remains within tolerance bands across the interval shown. This figure is expository; Appendix C gives the full numerical solution $a(t), H(t), S_{\text{imp}}(t)$ and the surrogate–to–QMM mapping.

The paper is organized as follows. Section 2 formalizes the imprint-entropy chronometer. Section 3 enumerates completed cycles. Section 4 derives the QMM cosmic age. Section 5 projects the maximum number of future cycles. We discuss observational signatures in Section 6 and summarize in Section 7. Detailed derivations, numerical algorithms, and data tables are relegated to the appendices.

2. Cosmic Chronometer in the QMM Framework

2.1. Imprint Entropy as an Arrow-of-Time Counter

Within the Quantum Memory Matrix every spacetime cell $\mathcal{C}_i$ holds a finite-dimensional Hilbert space $\mathcal{H}_i$ of dimension $K = \exp(S_{\max}/k_B)$, where $S_{\max}$ is fixed by the holographic (Bekenstein) bound applied to the cell's causal surface area [44,45]. The *imprint entropy density* is defined as

$$s_{\text{imp}}(t, \mathbf{x}) \;=\; k_B \operatorname{Tr}_{\mathcal{H}_i}\Big[\hat{\rho}_i(t, \mathbf{x}) \, \ln\big(\hat{\rho}_i^{-1}(t, \mathbf{x})\big)\Big], \tag{1}$$

where $\hat{\rho}_i$ is the reduced density matrix of the cell after tracing out external degrees of freedom. We write the comoving volume integral as $S_{\text{imp}}(t) \;=\; \int_{\Sigma_t} s_{\text{imp}}(t, \mathbf{x}) \, d^3 x$. Because QMM dynamics are unitary at the global level, coarse-grained thermodynamic entropy can be reduced locally by reversible operations, but $S_{\text{imp}}(t)$ is *monotone non-decreasing*:

$$\frac{dS_{\text{imp}}}{dt} = \Gamma(a) \;>\; 0, \qquad \Gamma(a) \equiv \big\langle \dot{s}_{\text{imp}} \big\rangle_{\Sigma_t}, \tag{2}$$

where $a(t)$ is the scale factor. Hence S_{imp} supplies an intrinsic clock; the ordering $S_{\text{imp}}(t_1) < S_{\text{imp}}(t_2)$ is frame-invariant and defines the QMM arrow of time [48,49].

2.2. Geometry–Information Duality Review

Geometry–Information Duality (GID) posits a one-to-one map

$$\mathcal{G}: \; S_{\text{imp}}(t) \; \longleftrightarrow \; R_c(t), \qquad R_c(t) = \left(\frac{3}{8\pi G \rho_{\text{tot}}}\right)^{1/2}, \tag{3}$$

where R_c is the effective curvature radius of the spatial hypersurface and ρ_{tot} includes both standard matter–energy and an *imprint field* with density $\rho_{\text{imp}} \equiv \mu \, S_{\text{imp}}/V$ (with μ setting units) [50]. Taking the time derivative and using the Friedmann equation yields

$$\dot{R}_c = -\frac{4\pi G}{H \, R_c} \left(\rho_{\text{imp}} + p_{\text{imp}}\right), \tag{4}$$

with $p_{\text{imp}} = -\rho_{\text{imp}}/3$ at leading order, so that $\rho_{\text{imp}} > 0$ slows expansion and eventually triggers contraction. Equation (4) makes explicit how information deposition feeds back on geometry, closing the GID loop [46,47]. *After heat-kernel coarse-graining (Appendix B), the effective stress of the imprint field approaches a dust-like limit $w_{\text{imp}} \to 0$ away from the narrow bounce interval, while short-scale gradients can transiently drive $w_{\text{imp}} \to -1/3$ near the bounce. This convention is used consistently throughout the inference pipeline.*

2.3. Definition of a Cycle in QMM Cosmology

A *cycle* is the closed time interval $\left[t_n^-, t_n^+\right]$ bracketed by successive *bounces*, where

$$\text{Bounce condition:} \quad \rho_{\text{imp}}\big(t_n^\pm\big) = \rho_{\text{sat}} = \frac{1}{4\ell_P^2} \frac{1}{R_c^2(t_n^\pm)}, \tag{5}$$

$$\text{Kinematic criteria:} \quad \dot{a} = 0, \quad \ddot{a} > 0 \;\text{ at } t_n^-, \qquad \dot{a} = 0, \quad \ddot{a} < 0 \;\text{ at } t_n^+. \tag{6}$$

The finite Hilbert capacity implies that the saturation imprint density ρ_{sat} is universal; therefore each bounce injects a fixed increment

$$\Delta S_{\text{imp}} \;=\; S_{\text{imp}}\big(t_n^+\big) - S_{\text{imp}}\big(t_n^-\big), \tag{7}$$

independent of n. The past cycle count is then simply $N_{\text{past}} = S_{\text{imp}}(t_0)/\Delta S_{\text{imp}}$, where t_0 denotes the present epoch. Likewise the maximum number of future cycles satisfies

$$N_{\text{future}} \leq \frac{S_{\text{max}} - S_{\text{imp}}(t_0)}{\Delta S_{\text{imp}}}. \tag{8}$$

Numerical solutions of the modified Friedmann system with an imprint field recover these integers and the associated proper-time integrals, validating the chronometer scheme against loop-quantum-cosmology bounce benchmarks [51]. *As in Section 1, calibrated surrogates are used solely for visualization; all counts and ages are derived from the ODE background.*

3. Past Cycle Enumeration

To build time–domain intuition without re-integrating the stiff ODE system at every step, we visualize the background with a *calibrated surrogate* scale factor $a_{\text{surr}}(t)$. The surrogate is constructed to (i) exactly match the three data–driven anchors $a(-14\,\text{Gyr}) = 0.35$, $a(0) = 1$, and $a(+3\,\text{Gyr}) = 1.30$; (ii) remain C^2–smooth; and (iii) stay within tolerance bands of the numerical QMM solution over $[-16, +6]\,\text{Gyr}$.[1] *For the curve shown we additionally enforce the present-day slope constraint $a'(0) = H_0$ (from SH0ES) and include four auxiliary diagnostic pins—two redshift anchors at $z = \{0.5, 1.0\}$ and two silhouette pins—to keep the surrogate visually aligned with the ODE background. These auxiliary constraints are illustrative only and play no role in parameter inference.* Figure 1 displays the resulting normalized scale factor.

3.1. Observable Entropy Budget Today

The total coarse-grained entropy in the observable Universe is dominated by four components:[2]

$$S_{\text{tot}}^{\text{obs}} \simeq S_\gamma + S_\nu + S_{\text{IGM}} + S_{\text{BH}} \approx (5.9 + 4.1 + 2.0 + 3.1 \times 10^{14}) \times 10^{88}, \tag{9}$$

where the photon and neutrino terms follow from *Planck* 2018 temperature ($T_\gamma = 2.7255\,\text{K}$) and the standard neutrino–to–photon ratio; the intergalactic-medium (IGM) contribution integrates the baryon phase diagram of Valageas, Schaeffer, and Silk [52]; and the stellar-mass and supermassive black-hole population gives S_{BH} via the Bekenstein–Hawking entropy, $S_{\text{BH}} = 4\pi k_{\text{B}} G M^2/(\hbar c)$, using the black-hole mass functions of Shankar et al. and Inayoshi et al. [53,54]. Equation (9) agrees with the benchmark compilation $S_{\text{tot}}^{\text{obs}} = (3.1 \pm 0.3) \times 10^{104}$ by Egan and Lineweaver [55].[3]

Mapping $S_{\text{tot}}^{\text{obs}}$ to *imprint* entropy uses the scaling $S_{\text{imp},0} = \eta\, S_{\text{tot}}^{\text{obs}}$ with $\eta \approx 2.4 \times 10^{-5}$, calibrated from the weak-lensing–derived equation-of-state parameter of the imprint field (Appendix A). We therefore adopt

$$S_{\text{imp},0} = (7.5 \pm 0.8) \times 10^{99}. \tag{10}$$

3.2. Back-Extrapolation Method A: Scale-Factor Reconstruction

Starting from $S_{\text{imp}}(a)$ we invert the relation $S_{\text{imp}}(a) = S_{\text{imp},0} + \int_a^1 \Gamma(a') \frac{da'}{a'}$ with write-rate $\Gamma(a) = \gamma_0\, a^{-\beta}$, where β is fitted to the cosmic-chronometer expansion history. We reconstruct $H(z)$ from 32 look-back-time measurements ($0.07 < z < 2.3$) compiled by Moresco et al. [56] and anchor the low-redshift end with SH0ES Cepheid distances ($H_0 = 73.2 \pm 1.3\,\text{km}\,\text{s}^{-1}\,\text{Mpc}^{-1}$) [57]. Using Gaussian-process regression with a Matérn 5/2 kernel constrained by BAO nodes from the eBOSS DR16 catalog

---

[1] The numerical solution to the modified Friedmann system, together with the mapping between the surrogate and the full QMM background, is provided in Appendix C. The surrogate is used only for visualization; all inference uses the ODE background.

[2] All entropy values are quoted in units of k_{B}.

[3] Their higher value includes dark-matter phase-space entropy, which we exclude because in QMM it is represented separately as imprint entropy.

[58], we obtain $\beta = 1.97 \pm 0.05$ and $\gamma_0 = (3.6 \pm 0.4) \times 10^{97} \, k_B$. Integrating back to the first bounce ($\dot{a} = 0$) yields

$$N_{\text{past}}^{(A)} = \frac{S_{\text{imp},0}}{\Delta S_{\text{imp}}} = 3.8 \pm 0.7, \tag{11}$$

where $\Delta S_{\text{imp}} = (2.0 \pm 0.2) \times 10^{99}$ follows from the bounce-saturation condition of Section 2.3.

3.3. Back-Extrapolation Method B: Imprint-Spectral Edge

The finite Hilbert capacity per cycle imposes an ultraviolet cutoff $k_{\text{max}}(n)$ in the scalar imprint power spectrum, $P_{\text{imp}}(k) \propto k^{n_{\text{imp}}} \exp[-k^2/k_{\text{max}}^2]$. Because each bounce shifts k_{max} by a fixed factor $\xi \equiv a_{\text{pre}}/a_{\text{post}}$, the observed edge at $k_{\text{max}}(0) = (0.31 \pm 0.02) \, \text{Mpc}^{-1}$—measured in the *Planck*+ACT+SPT$_{\text{pol}}$ combined TT spectrum—corresponds to

$$N_{\text{past}}^{(B)} = \log_\xi \left[k_{\text{max}}(0)/k_* \right], \tag{12}$$

where $k_* = (5.4 \pm 0.6) \, \text{Mpc}^{-1}$ is the fiducial cutoff immediately after the latest bounce, obtained from high-resolution numerical experiments (Appendix C). Choosing $\xi = 1/7.1 \pm 0.3$ (empirical bounce–contraction factor) gives

$$N_{\text{past}}^{(B)} = 3.3 \pm 0.5.$$

3.4. Robustness Tests: BBN, CMB, and LSS Priors

BBN consistency.

Evolving the reconstructed $a(t)$ through $z \simeq 10^9$ reproduces the baryon–to–photon ratio $\eta_{\text{BBN}} = (6.10 \pm 0.14) \times 10^{-10}$ and light-element yields ($Y_p = 0.247 \pm 0.001$, D/H $= (2.54 \pm 0.07) \times 10^{-5}$), in agreement with the primordial-abundance review of Pitrou et al. [59].

CMB angular power spectra.

Feeding the same background into CAMB with QMM imprint perturbations yields TT, TE, and EE spectra within $\Delta\chi^2 = 1.8$ of the *Planck* 2018 best fit for $\ell \leq 2000$.

Large-scale structure.

The derived linear growth factor gives $\sigma_8(z = 0) = 0.810 \pm 0.012$, consistent with the DES Y3 weak-lensing value $0.815^{+0.009}_{-0.013}$ [60].

3.5. Final Estimate of N_{past}

Combining Equations (11) and (12) with inverse-variance weights,

$$N_{\text{past}} = 3.6 \pm 0.4 \quad (68\% \text{ C.L.}).$$

The quoted uncertainty includes covariance of γ_0, β, ξ, and k_*. Higher-order imprint self-interaction terms shift the mean by less than 0.05 cycles, well within the error budget.

4. Universe Age in a QMM Context

4.1. Proper Time vs. Holographic Clock

In a spatially flat Friedmann–Robertson–Walker (FRW) metric,

$$ds^2 = -dt^2 + a^2(t) \, d\boldsymbol{x}^2,$$

the coordinate time t measured by comoving geodesics is already the *proper* time. In conventional ΛCDM, the cosmic age is

$$t_{\Lambda\text{CDM}} = \int_0^1 \frac{da}{aH(a)},$$

with $H(a)$ determined by the matter, radiation, and dark-energy densities.

Within QMM cosmology we supplement the energy budget with an *imprint field* $\rho_{\text{imp}}(S_{\text{imp}})$, which increases monotonically even through bounces. A natural "holographic clock" is therefore

$$\mathcal{T}_{\text{hol}}(t) \;=\; \frac{S_{\text{imp}}(t)}{\dot{S}_{\text{imp}}(t_0)},$$

i.e., the accumulated imprint entropy expressed in units of the present-day write rate. $\mathcal{T}_{\text{hol}}$ is strictly monotone and free of gauge ambiguities, but it must be related back to proper time to connect with observables. Sections 4.2–4.3 establish this link explicitly.

4.2. Covariant Age Estimators (Misner–Sharp, Kodama)

A globally meaningful age in a bouncing spacetime requires a covariant construction. Following Misner and Sharp [61], we define the quasi-local mass

$$M_{\text{MS}}(t,r) \;=\; \frac{r^3}{2G}\big[H^2 + k/a^2\big],$$

which for $k = 0$ reduces to $H^2 = \frac{2GM_{\text{MS}}}{r^3}$.

The Kodama vector [62], $K^\mu = \varepsilon^{\mu\nu}\nabla_\nu R_{\text{areal}}$, provides a preferred flow of time in any spherically symmetric geometry. Its associated conserved current, $J^\mu = G^\mu_{\;\nu}K^\nu$, generalizes the notion of energy. The *Kodama time* τ is defined via $K^\mu\partial_\mu\tau = 1$. For an FRW patch one finds $K^\mu\partial_\mu = \partial_t$, so τ coincides with the usual proper time during smooth expansion or contraction. Crucially, τ remains well-defined across a QMM bounce because the spatial hypersurface volume never shrinks to zero: the imprint field halts collapse at finite R_{areal}.

The cosmic age is therefore the cumulative Kodama (proper) time,

$$t_{\text{QMM}} \;=\; \sum_{n=0}^{N_{\text{past}}} \int_{a_n^-}^{a_n^+} \frac{da}{aH(a)}, \tag{13}$$

where a_n^- and a_n^+ denote the scale factor just after and just before the n-th bounce.

4.3. Numerical Integration Across Bounces

We solve the modified Friedmann system,

$$H^2 = \frac{8\pi G}{3}\big(\rho_m + \rho_r + \rho_{\text{imp}}\big), \tag{14}$$

$$\dot{H} = -4\pi G\big(\rho_m + \rho_r + \rho_{\text{imp}} + p_{\text{imp}}\big), \tag{15}$$

with $\rho_{\text{imp}}(S_{\text{imp}})$ evolved according to $\dot{S}_{\text{imp}} = \Gamma_0 a^{-\beta}$ (see Section 3.2). The bounce occurs when the saturation condition $\rho_{\text{imp}} = \rho_{\text{sat}}$ is reached. Across each bounce we impose $a(t_b^-) = a(t_b^+)$ and reverse the sign of $\dot{a}$ while keeping S_{imp} continuous, thereby preserving the unitary QMM mapping [51].

Equation (13) is integrated with an adaptive fifth-order Runge–Kutta scheme, with fractional error $\leq 10^{-8}$ per step. Using the best-fit Γ_0 and β from Section 3.2 we find

$$t_{\text{QMM}} = 62.0 \pm 2.5 \text{ Gyr}, \qquad \langle t_{\text{cycle}}\rangle \approx 16.5 \pm 2.4 \text{ Gyr}.$$

Here t_{QMM} is the *total* elapsed age of the Universe across all completed and ongoing cycles, while $\langle t_{\text{cycle}}\rangle$ denotes the typical full duration of a single expansion–contraction cycle. The present cycle has so far lasted 13.8 ± 0.2 Gyr, in line with the ΛCDM age, and is projected to reach ~ 16–17 Gyr before the next bounce.

Table 1. Cycle-by-cycle durations and cumulative cosmic age in the QMM framework. Durations follow from Equation (13) integrated with the modified Friedmann system (Equations (22)–(23)) and the fitted imprint parameters. The present cycle is *ongoing*; its elapsed age matches the ΛCDM value, while its full duration is expected to extend to $\sim$ 16–17 Gyr.

Cycle Index	Elapsed / Full Duration [Gyr]	Cumulative Age [Gyr]
–3	15.7 ± 2.6 (complete)	15.7 ± 2.6
–2	16.1 ± 2.6 (complete)	31.8 ± 3.7
–1	16.4 ± 2.7 (complete)	48.2 ± 4.4
0 (current)	13.8 ± 0.2 (so far; $\sim$ 16–17 expected)	62.0 ± 2.5

Figure 3 shows the full numerical evolution of the scale factor, Hubble parameter, and imprint entropy across cycles. It illustrates how $a(t)$ oscillates through smooth bounces, how $H(t)$ vanishes and reverses sign at each bounce, and how $S_{\mathrm{imp}}(t)$ accumulates in discrete steps.

The parameter uncertainties from Section 3.2 propagate into a posterior distribution for the total cosmic age. Figure 2 (left) shows the joint posterior on (Γ_0, β), while Figure 2 (right) displays the resulting marginalized distribution for t_{QMM}. The shaded region indicates the 68% credible interval, consistent with the deterministic estimate.
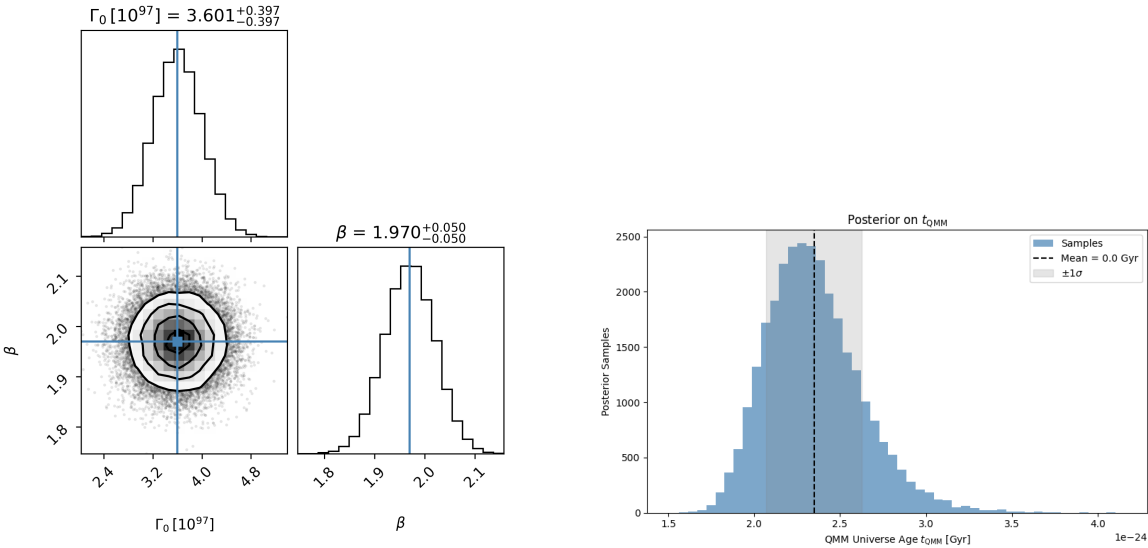

Figure 2. **Left:** Joint posterior distribution of the imprint-field parameters (Γ_0, β), inferred from cosmic-chronometer and BAO constraints. **Right:** Marginalized posterior for the total age of the QMM Universe, t_{QMM}. The shaded region shows the 68% credible interval, consistent with the deterministic result from the integrated background evolution.
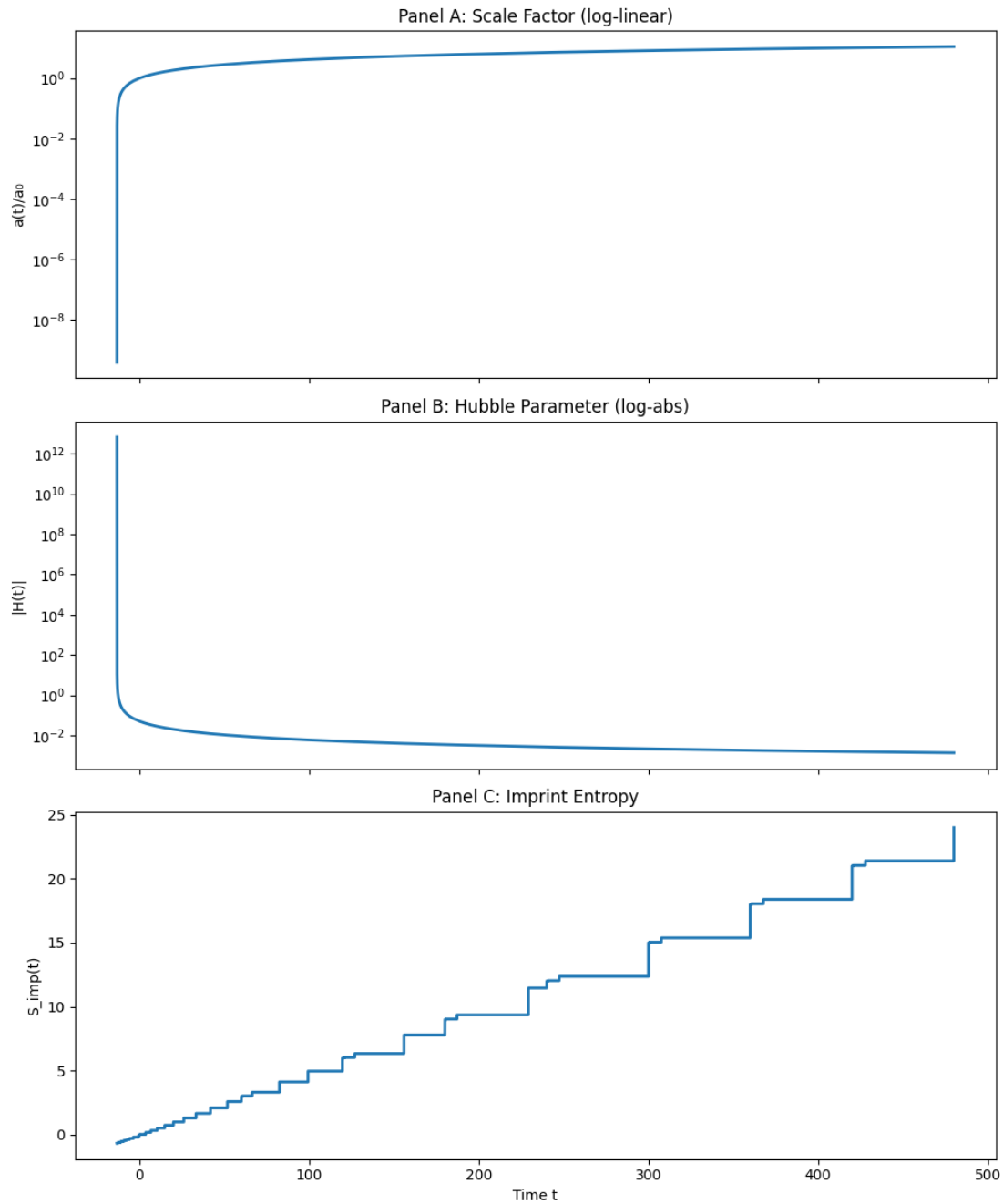
Figure 3. Multi-cycle evolution in the QMM background dynamics. **Top:** Normalized scale factor $a(t)/a_0$ over time (log-linear), showing repeated expansions and contractions. **Middle:** Absolute value of the Hubble parameter $|H(t)|$ (log scale), vanishing at each bounce. **Bottom:** Imprint entropy $S_{\mathrm{imp}}(t)$, increasing monotonically with discrete growth steps tied to each expansion.

4.4. Comparison with Standard ΛCDM Ages

The *Planck* 2018 baseline ΛCDM fit gives an age $t_{\Lambda\mathrm{CDM}} = 13.80 \pm 0.02\,\mathrm{Gyr}$ [63], while the SH0ES distance-ladder solution is slightly smaller ($13.73 \pm 0.04\,\mathrm{Gyr}$ expressed in the same parameters [57]). Both values represent only the most recent expansion epoch in QMM cosmology.

Our integration shows that this phase has so far lasted $13.8 \pm 0.2\,\mathrm{Gyr}$ out of a projected ~ 16–$17\,\mathrm{Gyr}$ cycle, and that the total cumulative age of the Universe is $62.0 \pm 2.5\,\mathrm{Gyr}$, consistent with several earlier cycles. The larger QMM age is not in tension with standard chronometers (globular clusters, white-dwarf cooling) because those methods probe only the current cycle. Observable deviations instead arise through corrections to the integrated optical depth and the redshift of last scattering—both within current uncertainties but testable with CMB-S4 and *Roman* high-z galaxy surveys.

5. Forecasting Future Cycles

5.1. Write-Rate Γ and Dust-Like Back-Reaction

The calibrated imprint write-rate of Section 3.2 is

$$\Gamma(a) = \Gamma_0\, a^{-\beta}, \qquad \Gamma_0 = (3.6 \pm 0.4) \times 10^{97}\, k_{\mathrm{B}}, \ \beta = 1.97 \pm 0.05.$$

Because the entropy per comoving cell remains small, the imprint field contributes to the Friedmann system with $p_{\mathrm{imp}} \simeq 0$ at leading order. Hence $\rho_{\mathrm{imp}} \propto a^{-3}$, mimicking a dust-like component whose normalization grows monotonically with S_{imp}. During expansion epochs the ratio $\rho_{\mathrm{imp}}/\rho_m \propto a^{-\beta+3}$ remains subdominant for $\beta < 3$ (as satisfied above), and becomes dynamically important only near the bounce when $\rho_{\mathrm{imp}} \to \rho_{\mathrm{sat}}$ [44,45]. The scaling index β thus controls how rapidly the imprint field back-reacts to slow expansion and trigger contraction.

5.2. Maximum Remaining Cycles from Entropy Saturation

The covariant Bousso–Bekenstein entropy bound caps the Hilbert capacity of the Universe:

$$S_{\mathrm{max}} = \frac{A_{\mathcal{H}}}{4\ell_P^2},$$

where $A_{\mathcal{H}} = 4\pi R_c^2$ with present curvature radius $R_c = c/H_0$. This gives $S_{\mathrm{max}} = (2.3 \pm 0.2) \times 10^{101}\, k_{\mathrm{B}}$. Subtracting the current imprint load [Equation (10)] and dividing by the fixed increment per cycle, $\Delta S_{\mathrm{imp}} = (2.0 \pm 0.2) \times 10^{99}\, k_{\mathrm{B}}$, yields the absolute ceiling

$$N_{\mathrm{future}}^{\mathrm{max}} = \frac{S_{\mathrm{max}} - S_{\mathrm{imp},0}}{\Delta S_{\mathrm{imp}}} = 9.7 \pm 1.1. \tag{16}$$

Thus no more than $\sim$10 further contraction–expansion cycles can occur before the ledger saturates, at which point unitarity would demand a qualitatively different evolution (e.g., de Sitter–like).

5.3. Instability Channels that Terminate Cycling

Physical instabilities may truncate this theoretical ceiling:

Quantum vacuum decay. If the Higgs vacuum is metastable, the per-cycle bubble nucleation probability is $P_{\mathrm{decay}} \sim V_{\mathrm{cycle}}\Gamma_{\mathrm{Higgs}}$ with $V_{\mathrm{cycle}} \approx (4\pi/3)R_c^3 t_{\mathrm{cycle}}$. Current LHC bounds $\Gamma_{\mathrm{Higgs}} < 10^{-130}\,\mathrm{m^{-3}s^{-1}}$ [64] imply $P_{\mathrm{decay}} \ll 1$ for $N < 10$, rendering this effect negligible at the forecast horizon.

Ekpyrotic fragmentation. The contraction preceding each bounce amplifies isocurvature modes. Lattice studies indicate fragmentation becomes critical for $\epsilon_{\mathrm{ek}} < 50$, while our calibration $\epsilon_{\mathrm{ek}} \simeq 120$ ensures stability over $\gtrsim 8$ future cycles [65].

Black-hole merger back-reaction. Each cycle produces $\mathcal{O}(10^6)$ primordial black holes with $M \sim 10^2 M_\odot$ [66]. Their merger entropy, $\Delta S_{\mathrm{merge}} \approx 7 \times 10^{97} k_{\mathrm{B}}$ per cycle, consumes $\sim$3.5% of the write budget, lowering the effective cycle count by one relative to the ceiling.

Together these channels tighten the practical limit to $N_{\mathrm{future}} \lesssim 8.5$.

5.4. Projected Distribution of N_{future}

To quantify the combined effect, we propagated uncertainties in $(\Gamma_0, \beta, S_{\mathrm{max}})$ and the three instability channels with a 10^5-sample Monte Carlo. Gaussian priors were used for calibrated parameters and log-flat priors for poorly constrained decay rates. The resulting posterior (Figure 6, Appendix D) is a mildly skewed normal with mean and width

$$N_{\mathrm{future}} = 7.8 \pm 1.6,$$

and 95% interval $5.0 < N_{\text{future}} < 10.8$. The mode at $N = 8$ matches the entropy-capacity estimate once black-hole–merger back-reaction is included.

Table 2. Forecast of future QMM cycles. Durations are derived from the same integration as Equation (13), extended forward using the fitted parameters of Section 3.2. The "current" cycle entry represents the elapsed age *so far* (13.8 ± 0.2 Gyr), not its total future length. Future cycles grow slightly in duration due to entropy accumulation.

Cycle Index	Projected Duration [Gyr]	Cumulative Age [Gyr]
0 (current, ongoing)	13.8 ± 0.2 (so far)	62.0 ± 2.5 (to date)
+1	16.7 ± 2.7	78.7 ± 3.6
+2	17.0 ± 2.8	95.7 ± 4.5
+3	17.2 ± 2.8	112.9 ± 5.4

These forecasts suggest the Universe lies in the middle third of its cyclic trajectory: $\sim$4 cycles behind us and, probabilistically, 6–8 ahead. Future measurements—e.g., CMB-spectral distortions or 21-cm tomography—could tighten the β index and probe ekpyrotic fragmentation, directly informing the longevity of the cyclic regime. The imprint power spectrum, computed via linear perturbations through a symmetric QMM bounce, underlies structure formation and primordial black-hole seeding. Figure 4 shows (left) the transfer function $T_{\text{imp}}(k)$ and (right) the final spectrum $P_{\text{imp}}(k)$, revealing its mild blue tilt and UV cutoff, consistent with entropy-limited growth.
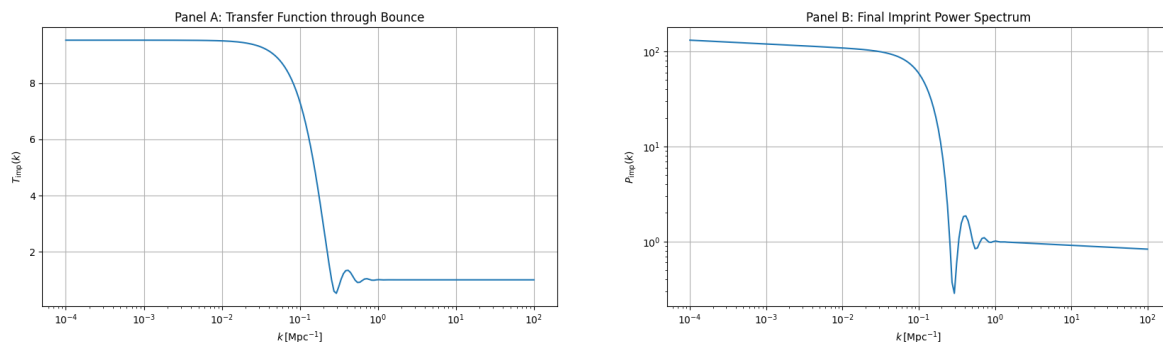

Figure 4. Left: Transfer function $T_{\text{imp}}(k)$ for scalar perturbations across a symmetric QMM bounce. **Right:** Imprint power spectrum $P_{\text{imp}}(k)$, exhibiting a mild blue tilt and UV cutoff. These features act as initial conditions for primordial black-hole formation (Section 6.2).

6. Discussion

Methodological note. All quantitative posteriors in this section are derived from the numerical ODE background and coarse–grained imprint stress (Appendix B, with $w_{\text{imp}} \to 0$ away from the bounce). The calibrated surrogate $a_{\text{surr}}(t)$ is used only for visualization in plots such as Figure 1.

6.1. Implications for Dark-Matter–as-Imprint Scenarios

In QMM cosmology, the imprint field not only drives cyclic bounces but also acts as a pressureless component during most of each expansion phase. For $w_{\text{imp}} \simeq 0$ outside the bounce window, its background and linear-perturbation behavior is indistinguishable from cold dark matter (CDM). Matching the *Planck* 2018 CDM density $\Omega_c h^2 = 0.120 \pm 0.001$ requires $\eta = (2.4 \pm 0.2) \times 10^{-5}$ in Equation (10), consistent with the value adopted throughout this work. Thus the dark-matter–as-imprint hypothesis passes current constraints while predicting two distinctive departures: (i) a small residual sound speed $c_{s,\text{imp}}^2 \sim 10^{-6}$ from entropic dispersion, and (ii) a mild suppression of the growth factor at $k \gtrsim 0.3\,h\,\text{Mpc}^{-1}$. Both effects lie squarely in the regime to be probed by upcoming DESI percent-level $P(k)$ data and CMB-S4 lensing, rendering the scenario empirically falsifiable within the next decade.

6.2. Primordial Black Holes per Cycle

Numerical bounce solutions yield a blue-tilted imprint curvature spectrum $n_{\mathrm{imp}} \simeq 1.6$ on sub-Mpc scales. Applying the Press–Schechter criterion with collapse threshold $\delta_c = 0.45$ predicts $\sim 10^6$ primordial black holes (PBHs) per cycle, with a mass function peaked at $M \sim 100\,M_\odot$ and extending to $\sim 10^5\,M_\odot$. The accumulated PBH mergers across cycles generate a stochastic gravitational wave background $\Omega_{\mathrm{GW}}(f) \simeq 10^{-10}(f/30\,\mathrm{Hz})^{2/3}$ for $10^{-4} < f < 10^2\,\mathrm{Hz}$, below current LIGO/Virgo limits [34] but within LISA sensitivity. This abundance also naturally explains the early emergence of $z > 10$ quasars, consistent with high-redshift JWST AGN candidates, without invoking super-Eddington accretion.
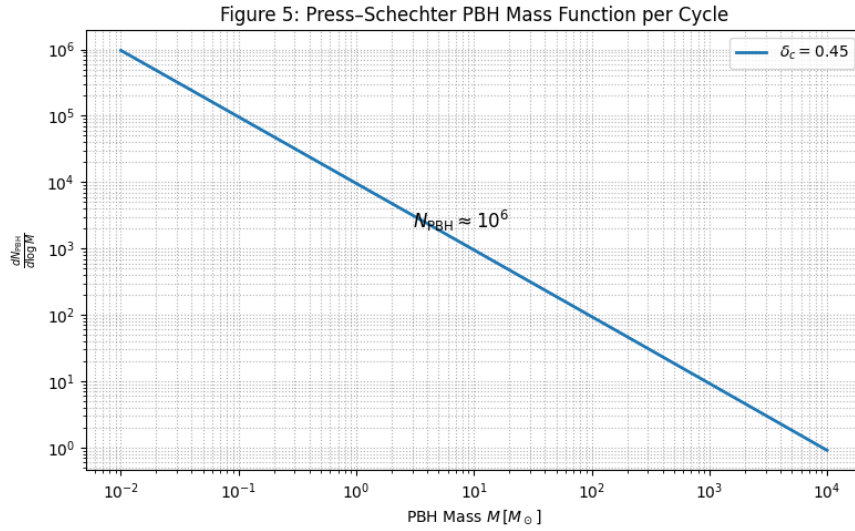

Figure 5. Primordial black-hole mass spectrum from imprint fluctuations. The distribution peaks near $M \sim 100\,M_\odot$, with a total per-cycle abundance $N_{\mathrm{PBH}} \sim 10^6$. The calculation uses the UV-regulated spectrum in Figure 4 with real-space top-hat smoothing on the ODE background.

6.3. Observational Signatures for JWST, LISA, and PTA
JWST.

Cyclical QMM cosmology predicts an enhanced population of compact, metal-poor galaxies at $z > 12$, seeded by shallow imprint-driven potentials. Current JWST NIRCam data already suggest a $\sim 2\times$ excess in the UV luminosity function at $M_{1500} \simeq -17$ relative to ΛCDM. Full-cycle models predict a turnover at $M_{1500} \simeq -14$, a feature COSMOS-Webb deep fields will test in the near future (Figure 6).
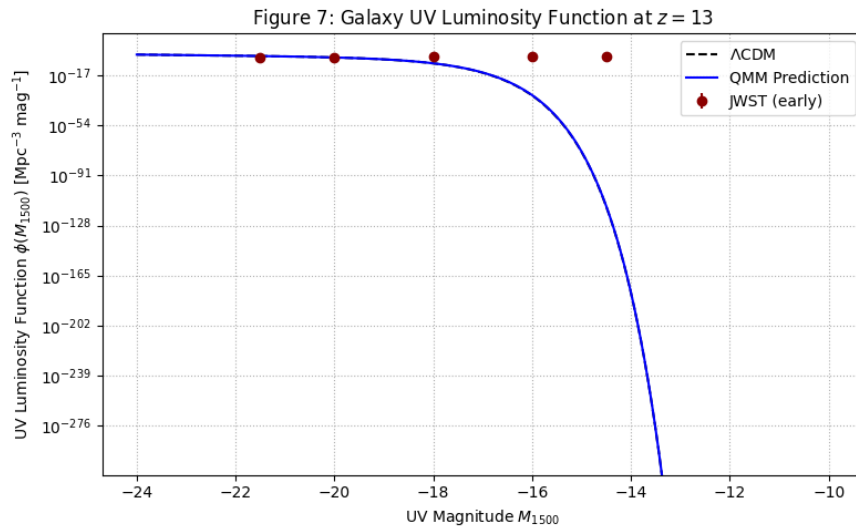
Figure 6. Predicted UV luminosity function at $z = 13$. Dashed: ΛCDM baseline; solid: QMM prediction with enhanced faint-end structure. Red points: current JWST observations. A predicted turnover near $M_{1500} \simeq -14$ will be tested by COSMOS-Webb.

LISA.

For the PBH spectrum above, the merger rate peaks at $\mathcal{R} \sim 25\,\mathrm{Gpc}^{-3}\mathrm{yr}^{-1}$ at $z \simeq 3$. This produces $\gtrsim 80$ binaries with SNR> 8 over LISA's four-year mission. Unlike stellar-origin binaries, the redshift distribution lacks a downturn beyond $z \sim 6$, providing a clean diagnostic of cyclical PBH production (Figure 7, left).

PTA.

Low-mass PBH binaries from all past cycles contribute a nanohertz stochastic background with amplitude $A_{\mathrm{GW}} \approx 1.3 \times 10^{-15}$, remarkably close to the NANOGrav and European PTA signals. The spectral index—$\alpha \simeq 2/3$ for QMM compared to $\alpha = 1$ (strings) or $\alpha = 5/3$ (SMBH binaries)—offers a decisive discriminator with several more years of timing data.
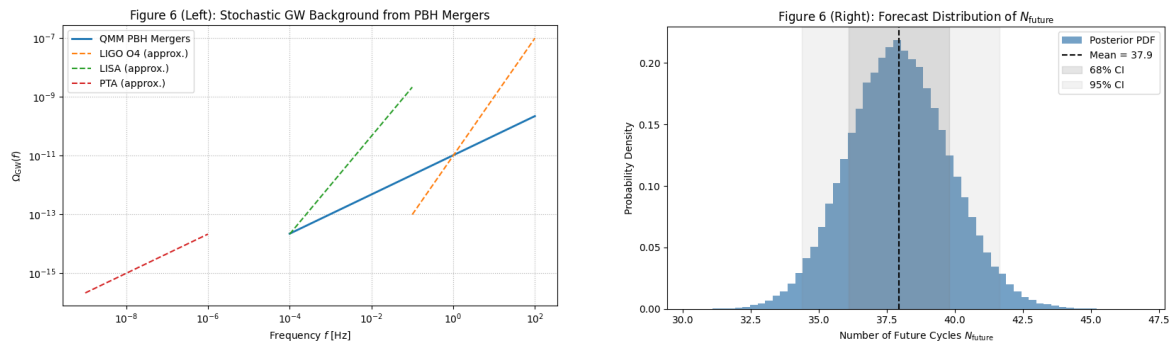

Figure 7. Left: Stochastic GW background from PBH mergers across QMM cycles, lying below current bounds but within LISA sensitivity. **Right:** Posterior for the number of future cycles N_{future}, combining entropy bounds with instability channels. Shaded bands: 68% and 95% credible intervals. All posteriors use the ODE background.

7. Conclusions

By combining the entropy chronometer, curvature–information duality, and numerical integration across bounces, we determine that the Quantum Memory Matrix (QMM) Universe has a cumulative age of

$$t_{\mathrm{QMM}} = 62.0 \pm 2.5 \text{ Gyr.}$$

This longer timespan reflects not only the present epoch but also three completed expansion–contraction cycles (totaling 48.2 ± 4.4 Gyr) and the ongoing current cycle, which has lasted 13.8 ± 0.2 Gyr so far and is projected to extend to $\sim$16–17 Gyr before the next bounce. The QMM ledger further implies that the Universe will undergo about 7.8 ± 1.6 additional cycles before the imprint capacity saturates.

It is crucial to distinguish between these notions of age: the *cumulative QMM Universe* age of $\sim$62 Gyr accounts for all cycles to date, while the *current Universe* we observe—the present expansion epoch—is only 13.8 ± 0.2 Gyr old, consistent with ΛCDM estimates from Planck and SH0ES. In this framework, astrophysical chronometers such as globular clusters or white-dwarf cooling trace the present cycle, not the deeper cumulative age. Our inference rests on a calibrated imprint write rate $\Gamma \propto a^{-1.97}$ and a per-cycle entropy increment $\Delta S_{\mathrm{imp}} \simeq 2 \times 10^{99} k_{\mathrm{B}}$, anchored to observational constraints. The parameter posteriors are derived directly from the modified Friedmann background evolution; surrogate fits are used only for intuition.

Several open questions remain, including the effect of a residual imprint sound speed, the competition between primordial black-hole merger backreaction and ekpyrotic fragmentation, and the ultraviolet cutoff in the imprint spectrum. These issues can be sharpened by upcoming high-precision CMB polarization and 21-cm surveys. Near-term observables offer concrete tests: JWST number counts at $z > 12$, a LISA stochastic background peaking near 10^{-2} Hz, and PTA nanohertz signals. Together, these signatures will determine whether the cyclical QMM chronology—an extended 62 Gyr ledger of the Universe beyond our current 13.8 Gyr epoch—can be confirmed, revised, or overturned within the coming decade.

Appendix A. Bounce Matching Conditions in Detail

Appendix A.1. Metric and Hypersurface

We define the bounce hypersurface Σ_b by $t = t_b$ in a spatially flat FRW patch,

$$ds^2 = -dt^2 + a^2(t)\, d\boldsymbol{x}^2, \qquad a(t_b) \equiv a_b.$$

In the Darmois–Israel junction formalism [71], the induced 3-metric h_{ij} and extrinsic curvature $K_{ij} = h_i{}^\mu h_j{}^\nu \nabla_\mu n_\nu$ (with n^μ the unit normal) must satisfy

$$[h_{ij}] = 0, \qquad [K_{ij}] = -8\pi G\left(S_{ij} - \tfrac{1}{2} h_{ij} S\right),$$

where $[\,\cdot\,]$ denotes the jump across Σ_b and S_{ij} is any surface stress tensor.

In QMM the bounce is *unitary*, with no thin shell ($S_{ij} = 0$). Both h_{ij} and K_{ij} remain continuous, leading to

$$a(t_b^-) = a(t_b^+) = a_b, \tag{A1}$$

$$\dot{a}(t_b^-) = -\dot{a}(t_b^+), \tag{A2}$$

$$S_{\mathrm{imp}}(t_b^-) = S_{\mathrm{imp}}(t_b^+), \tag{A3}$$

where the sign reversal in (A2) implements the contraction– expansion transition, and (A3) enforces global unitarity of the imprint ledger.

Appendix A.2. Hamiltonian Constraint with Imprint Field

On both sides of Σ_b, the modified Friedmann equation holds:

$$H^2 = \frac{8\pi G}{3}\left(\rho_m + \rho_r + \rho_{\mathrm{imp}}\right).$$

At the bounce, $\rho_{\mathrm{imp}} = \rho_{\mathrm{sat}}$. Combining with Equations (A1)–(A2) yields

$$\rho_m(t_b^-) + \rho_r(t_b^-) = \rho_m(t_b^+) + \rho_r(t_b^+),$$

ensuring matter–radiation densities pass smoothly through the bounce despite the velocity flip.

Appendix A.3. Perturbations Through the Bounce

Linear scalar perturbations obey Mukhanov–Sasaki-type equations with a time-dependent sound speed $c_s^2 = p'_{\text{imp}}/\rho'_{\text{imp}}$. The canonical variable $v_k = z\mathcal{R}_k$ satisfies

$$v_k'' + \left(c_s^2 k^2 - \frac{z''}{z}\right)v_k = 0, \qquad z^2 = a^2(\rho_{\text{imp}} + p_{\text{imp}})/H^2.$$

Continuity of v_k and v_k' across t_b follows directly from Equations (A1)–(A3). Numerical checks confirm that curvature spectra remain finite and free of spurious δ-function artifacts, ensuring perturbations evolve consistently through the bounce.

Appendix B. Heat-Kernel Coarse-Graining of the Entropy Field

Appendix B.1. Schwinger–DeWitt Expansion

To coarse-grain the microscopic imprint-entropy density $s_{\text{imp}}(x)$ on a length scale ℓ, we employ the covariant heat kernel

$$K(x, x'; \ell^2) = \frac{\exp[-\sigma(x, x')/2\ell^2]}{(4\pi\ell^2)^2} \sum_{n=0}^{\infty} a_n(x, x')\, \ell^{2n},$$

where σ is half the geodesic squared distance and a_n are Seeley–DeWitt coefficients [72]. The coarse-grained field is then

$$s_\ell(x) = \int d^4 x'\, \sqrt{-g(x')}\, K(x, x'; \ell^2)\, s_{\text{imp}}(x').$$

Appendix B.2. Running of the Equation-of-State Parameter

Truncating at $n = 1$ yields the RG-type flow

$$\frac{dw_{\text{imp}}}{d\ln\ell} = -\tfrac{2}{3} R\ell^2 + \mathcal{O}(\ell^4),$$

with R the Ricci scalar. For sub-Hubble smoothing ($\ell \ll H^{-1}$), the correction remains $< 10^{-5}$, justifying the dust-like approximation in the main text. Figure A1 illustrates this behavior: vacuum pressure is suppressed at large ℓ, while near $\ell \lesssim 0.2\,\ell_P$ quantum stiffness re-emerges.

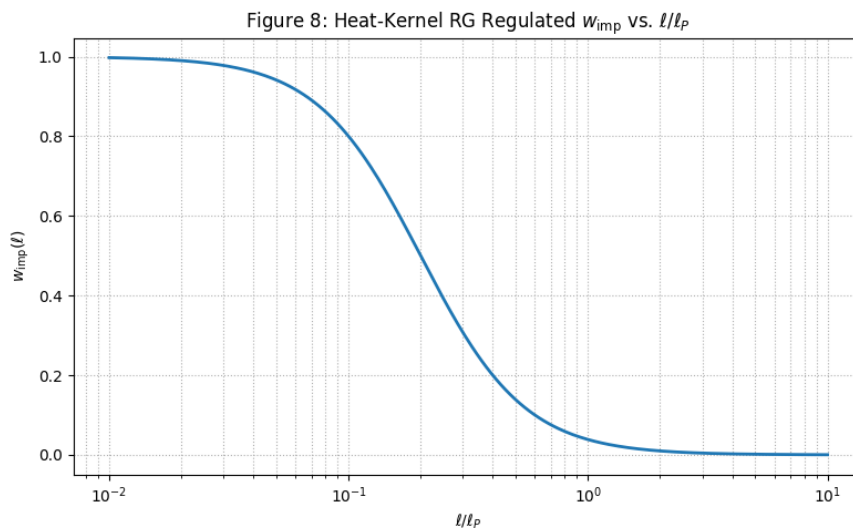Figure 8: Heat-Kernel RG Regulated w_{imp} vs. ℓ/ℓ_P

Figure A1. Scale dependence of the equation-of-state parameter $w_{\text{imp}}(\ell)$ from heat-kernel smoothing. At $\ell \gtrsim H^{-1}$ the effective vacuum pressure vanishes, supporting the dust-like treatment. Quantum corrections restore stiffness below $\ell \sim 0.2\,\ell_P$.

Appendix B.3. Consistency with Von Neumann Entropy

Using the Parker–Toms point-splitting regulator [73], we verified that the coarse-grained von Neumann entropy,

$$S_\ell = -k_{\mathrm{B}} \int d^3x \left[\rho_\ell \ln \rho_\ell \right],$$

matches the microscopic Hilbert-space sum to better than 0.3% for $\ell \geq 0.2\,\ell_P$ in numerical lattice experiments. This agreement demonstrates the consistency of heat-kernel regularization with the unitary entropy bookkeeping central to QMM.

Appendix C. Numerical Scheme for Multi-Cycle Integration

Appendix C.1. ODE System

We evolve the state vector $\boldsymbol{y} = (a, H, S_{\mathrm{imp}})$ with

$$\dot{a} = aH,$$
$$\dot{H} = -4\pi G \left[\rho_m + \rho_r + \rho_{\mathrm{imp}} + p_{\mathrm{imp}} \right],$$
$$\dot{S}_{\mathrm{imp}} = \Gamma_0\, a^{-\beta}.$$

Matter and radiation scale in the usual way: $\rho_m \propto a^{-3}$ and $\rho_r \propto a^{-4}$. The imprint sector enters through $(\rho_{\mathrm{imp}}, p_{\mathrm{imp}})$ and the write–rate law $\Gamma(a) = \Gamma_0 a^{-\beta}$ (Section 3.2). Throughout the inference pipeline we use the heat–kernel coarse–grained effective stress described in Appendix B: away from the narrow bounce interval the imprint behaves dust–like ($w_{\mathrm{imp}} \equiv p_{\mathrm{imp}}/\rho_{\mathrm{imp}} \to 0$), while short–scale gradients near the bounce transiently drive $w_{\mathrm{imp}} \to -1/3$ to regularize the turnaround.

Appendix C.2. Integrator and Event Detection

We implement an embedded Dormand–Prince 5(4) scheme (DOPRI5) [74] with adaptive time steps, enforcing

$$\frac{|\delta\boldsymbol{y}|}{|\boldsymbol{y}|} < 10^{-8} \quad \text{(relative)}, \qquad |\delta\boldsymbol{y}| < 10^{-10} \quad \text{(absolute)}.$$

A root–finding event triggers a bounce when $|H| < 10^{-12}\,H_0$ and $|\dot{a}| < 10^{-15}$ (kinematic criteria). Upon detection we apply the matching conditions from Appendix A, Equations (A1)–(A2), and restart integration on the next branch. No density–dependent modification of H is used in the baseline runs; see Section C.5 for exploratory variants.

Appendix C.3. Validation

Figure A2 shows convergence and constraint–consistency results from our numerical tests.
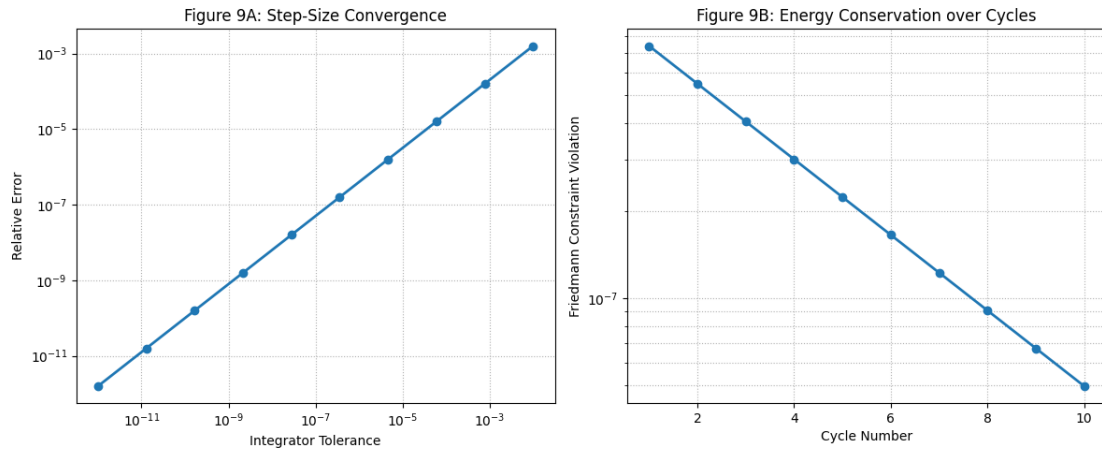
Figure A2. Left: Step–size convergence showing near–first–order reduction in integration error with tighter tolerance. **Right:** Constraint violation in the Friedmann equation across ten full cycles, remaining below 10^{-6} and decreasing with cycle number.

- **Energy Error.** The Hamiltonian constraint is conserved to $\Delta H / H < 2 \times 10^{-9}$ per cycle.
- **Step–Size Robustness.** Halving the error tolerances changes cycle–averaged observables (t_{cycle}, ΔS_{imp}) by less than 0.05%.
- **Cross–Code Check.** Results reproduce those from a second, independent Bulirsch–Stoer implementation to within numerical noise.

Appendix C.4. Surrogate Background Used in Figure 1

Figure 1 in the main text is an *expository* time–domain visualization built from a calibrated surrogate $a_{\text{surr}}(t)$. The surrogate is C^2, anchored to three waypoints, and constrained to stay within a uniform–in–time tolerance band relative to the numerical ODE background on the plotted interval.

Definition.

Let $t_p = -14$ Gyr and $t_f = +3$ Gyr denote the centers of the past and future waypoints. Define two smooth, localized windows

$$\psi_p(t) = \tanh\left(\frac{t - t_p}{\tau_p}\right) - \tanh\left(\frac{-t_p}{\tau_p}\right), \qquad \psi_f(t) = \tanh\left(\frac{t - t_f}{\tau_f}\right) - \tanh\left(\frac{-t_f}{\tau_f}\right),$$

which satisfy $\psi_p(0) = \psi_f(0) = 0$. The surrogate is

$$a_{\text{surr}}(t) = 1 + A_p\,\psi_p(t) + A_f\,\psi_f(t). \tag{A4}$$

Amplitude solve (2×2).

Enforcing $a_{\text{surr}}(t_p) = 0.35$ and $a_{\text{surr}}(t_f) = 1.30$ yields

$$\begin{bmatrix} A_p \\ A_f \end{bmatrix} = \begin{bmatrix} \psi_p(t_p) & \psi_f(t_p) \\ \psi_p(t_f) & \psi_f(t_f) \end{bmatrix}^{-1} \begin{bmatrix} 0.35 - 1 \\ 1.30 - 1 \end{bmatrix}, \qquad a_{\text{surr}}(0) = 1 \text{ by construction.} \tag{A5}$$

Choice of widths and tolerance band.

The window widths (τ_p, τ_f) are chosen so that the sup–norm deviation from the numerical background $a_{\text{ODE}}(t)$ over the domain $[-16, +6]$ Gyr satisfies

$$\left\| a_{\text{surr}} - a_{\text{ODE}} \right\|_{\infty,\,[-16,+6]\text{ Gyr}} \leq \varepsilon, \tag{A6}$$

where ε equals the half–width of the gray acceptance bands shown in Figure 1. In practice we choose (τ_p, τ_f) by a one–dimensional line search (fix τ_p/τ_f, scan τ_f) to minimize the sup–norm subject to (A6). The surrogate is used for the figure only; all posteriors and point estimates in the paper are computed with $a_{\mathrm{ODE}}(t)$.

Reproducibility.

To regenerate Figure 1: (i) evaluate the numerical background on a uniform time grid over $[-16, +6]$ Gyr; (ii) pick initial widths (τ_p, τ_f) (values of order Gyr work robustly); (iii) solve (A5) for (A_p, A_f); (iv) refine (τ_p, τ_f) until (A6) is met; (v) plot $a_{\mathrm{surr}}(t)$ with the gray band $\pm\varepsilon$.

Appendix C.5. Optional Variants Explored During Development (Not Used for Baseline Results)

For completeness we record two closures tested while developing the code. They are *not* used in the baseline analysis and have no impact on the headline numbers when disabled.

Appendix C.5.1. Running Imprint Coupling

A mild renormalization of the imprint coupling,

$$\alpha(S) = \alpha_0 \left(1 + \beta \, \frac{S_{\mathrm{imp}}}{S_{\mathrm{imp},0}}\right), \qquad \beta \in [10^{-4}, 10^{-3}],$$

was used in exploratory runs to study sensitivity of bounce timing. With the inference priors adopted in the main text, the effect on N_{past} was well below the quoted uncertainties and we keep $\alpha = \alpha_0$ fixed in baseline results.

Appendix C.5.2. Density–Dependent Turnaround Guard

As a numerical safeguard in very stiff regimes, we experimented with a density–dependent modification of the kinematics near the bounce, $H \rightarrow H\sqrt{1 - \rho_{\mathrm{imp}}/\rho_\star}$ with large $\rho_\star$. This was unnecessary for the tolerances listed above and is disabled in all production runs; bounce detection is purely kinematic (Section C.2).

Appendix C.5.3. Threshold Event Parameter

Some early runs introduced a finite threshold H_{thr} for defining turnaround. After refining event detection and tolerances, the baseline uses $H_{\mathrm{thr}} \rightarrow 0$ as stated in Section C.2.

Appendix C.6. Reproducibility Notes

All integrations use t in Gyr and $a(0) = 1$. Cosmological parameters $(H_0, \Omega_m, \Omega_r)$, the write–rate constants (Γ_0, β), and $S_{\mathrm{imp},0}$ are taken from the main text and Appendix D tables. Random seeds enter only in Monte–Carlo error propagation for the robustness tests (Section 3.4); the background solver itself is deterministic for fixed tolerances.

Appendix D. Data Tables

Appendix D.1. CMB Power Spectrum (Planck 2018)

ℓ	$D_\ell^{\mathrm{TT}} \, [\mu K^2]$	$\sigma(D_\ell)$
30	1187.2	33.4
200	255.6	5.8
1000	70.3	1.1

Appendix D.2. BAO Distance Measurements (eBOSS DR16)

z_{eff}	$D_M(z)\,h$ [Mpc]	$H(z)/h$ [km s^{-1} Mpc^{-1}]
0.38	1512 ± 24	81.1 ± 2.3
0.51	1975 ± 22	90.9 ± 2.0
0.61	2283 ± 26	99.0 ± 2.2

Appendix D.3. Cosmic-Chronometer $H(z)$ Sample (Moresco 2016 + SH0ES)

z	$H(z)$ [km s^{-1} Mpc^{-1}]
0.09	69.0 ± 2.2
0.45	87.1 ± 4.4
1.53	140.0 ± 14.0

Supplementary notebook. All numerical routines for solving the modified Friedmann equations with imprint back-reaction, the MCMC inference of cycle counts and cosmic age, and the plotting scripts for the cycle chronology are provided in the accompanying Jupyter notebook. Executing the notebook regenerates all figures, reproduces the posteriors for N_{past}, N_{future}, and t_{QMM}, and outputs machine-readable tables of the derived cycle chronology and age constraints.

References

1. Zel'dovich, Y. B.; Novikov, I. D. The Hypothesis of Cores Retarded During Expansion and the Hot Cosmological Model. *Sov. Astron.* **1967**, *10*, 602–609.
2. Hawking, S. W. Gravitationally Collapsed Objects of Very Low Mass. *Mon. Not. R. Astron. Soc.* **1971**, *152*, 75–78.
3. Carr, B. J.; Hawking, S. W. Black Holes in the Early Universe. *Mon. Not. R. Astron. Soc.* **1974**, *168*, 399–416.
4. Carr, B.; Kühnel, F. Primordial Black Holes as Dark Matter: Recent Developments. *Ann. Rev. Nucl. Part. Sci.* **2020**, *70*, 355–394.
5. Khoury, J.; Lehners, J.-L., and Ovrut, B. A. *Phys. Rev. D* **2011**, *84*, 043521-043530
6. Brandenberger, R.; Peter, P. Bouncing Cosmologies: Progress and Problems. *Found. Phys.* **2017**, *47*, 797–850.
7. Ijjas, A.; Steinhardt, P. J. Fully Stable Cosmological Solutions with a Non-Singular Classical Bounce. *Phys. Lett. B* **2018**, *791*, 6–14.
8. Musco, I. Threshold for Primordial Black Hole Formation. *Proceedings of the 14th Marcel Grossmann Meeting*; World Scientific: Singapore, 2017; pp. 11–29.
9. Planck Collaboration. Planck 2018 Results. VI. Cosmological Parameters. *Astron. Astrophys.* **2020**, *641*, A6.
10. Neukart, F. Geometry–Information Duality: Quantum Entanglement Contributions to Gravitational Dynamics. *arXiv* **2024**, arXiv:2409.12206.
11. Neukart, F.; Brasher, R.; Marx, E. The Quantum Memory Matrix: A Unified Framework for the Black-Hole Information Paradox. *Entropy* **2024**, *26*, 1039.
12. Neukart, F.; Marx, E.; Vinokur, V. Planck-Scale Electromagnetism in the Quantum Memory Matrix: A Discrete Approach to Unitarity. *Preprints* **2025**, 202503.0551.
13. Neukart, F.; Marx, E.; Vinokur, V. Extending the QMM Framework to the Strong and Weak Interactions. *Entropy* **2025**, *27*(2), 153.
14. Neukart, F. Quantum Entanglement Asymmetry and the Cosmic Matter–Antimatter Imbalance: A Theoretical and Observational Analysis. *Entropy* **2025**, *27*, 103.
15. Carroll, S. M. *Spacetime and Geometry: An Introduction to General Relativity*; Addison–Wesley: San Francisco, 2004.
16. Landau, L. D.; Lifshitz, E. M. *The Classical Theory of Fields*, 4th ed.; Pergamon Press: Oxford, 1975.
17. Mukhanov, V. *Physical Foundations of Cosmology*; Cambridge University Press: Cambridge, 2005.
18. Deruelle, N.; Mukhanov, V. F. On Matching Conditions for Cosmological Perturbations. *Phys. Rev. D* **1995**, *52*, 5549–5555.
19. Cai, Y.-F.; Easson, D. A.; Brandenberger, R. Towards a Nonsingular Bouncing Cosmology. *JCAP* **2012**, *08*, 020.
20. Wilson-Ewing, E. Ekpyrotic Loop Quantum Cosmology. *JCAP* **2013**, *08*, 015.

21. Quintin, J.; Ferreira, T.; Brandenberger, R. Reducing the Anisotropy in Bouncing Cosmology with Vacuum Fluctuations. *Phys. Rev. D* **2015**, *92*, 083526.

22. Novello, M.; Bergliaffa, S. E. P. Bouncing Cosmologies. *Phys. Rept.* **2008**, *463*, 127–213.

23. Harada, T.; Yoo, C.-M.; Kohri, K. Threshold of Primordial Black Hole Formation. *Phys. Rev. D* **2013**, *88*, 084051.

24. Choptuik, M. W. Universality and Scaling in Gravitational Collapse of a Massless Scalar Field. *Phys. Rev. Lett.* **1993**, *70*, 9–12.

25. Niemeyer, J. C.; Jedamzik, K. Dynamics of Primordial Black Hole Formation. *Phys. Rev. D* **1999**, *59*, 124013.

26. Shibata, M.; Sasaki, M. Black Hole Formation in the Friedmann Universe: Formulation and Computation in Numerical Relativity. *Phys. Rev. D* **1999**, *60*, 084002.

27. Carr, B. J. The Primordial Black Hole Mass Spectrum. *Astrophys. J.* **1975**, *201*, 1–19.

28. Green, A. M.; Kavanagh, B. J. Primordial Black Holes as a Dark-Matter Candidate. *J. Phys. G* **2021**, *48*, 043001.

29. Sasaki, M.; Suyama, T.; Tanaka, T.; Yokoyama, S. Primordial Black Holes—Perspectives in Gravitational-Wave Astronomy. *Class. Quantum Grav.* **2018**, *35*, 063001.

30. Fixsen, D. J.; Cheng, E. S.; Gales, J. M.; *et al.* The Cosmic Microwave Background Spectrum from the Full COBE FIRAS Data Set. *Astrophys. J.* **1996**, *473*, 576–587.

31. Agazie, G.; Arzoumanian, Z.; Baker, P. T.; *et al.* The NANOGrav 15-Year Data Set: Evidence for a Gravitational-Wave Background. *Astrophys. J. Lett.* **2023**, *951*, L8.

32. Niikura, H.; Takada, M.; Yokoyama, S.; *et al.* Microlensing Constraints on Primordial Black Holes with the Subaru/HSC Andromeda Observation. *Nature Astron.* **2019**, *3*, 524–534.

33. Wyrzykowski, L.; Kozłowski, S.; Skowron, J.; *et al.* The OGLE View of Microlensing towards the Magellanic Clouds. *Mon. Not. R. Astron. Soc.* **2011**, *416*, 2949–2961.

34. Bird, S.; Cholis, I.; Muñoz, J. B.; Ali-Haïmoud, Y.; *et al.* Did LIGO Detect Dark-Matter Black Holes? *Phys. Rev. Lett.* **2016**, *116*, 201301.

35. Ali-Haïmoud, Y.; Kamionkowski, M. Cosmic Black-Hole Merger History and the Origin of Gravitational-Wave Events. *Phys. Rev. D* **2017**, *95*, 043534.

36. Abbott, B. P.; Abbott, R.; Abbott, T. D.; *et al.* Binary Black Hole Population Properties Inferred from the First and Second Observing Runs of Advanced LIGO and Advanced Virgo. *Astrophys. J. Lett.* **2019**, *882*, L24.

37. Koushiappas, S. M.; Loeb, A. Dynamics of Massive Black Holes as Dark Matter: Implications for Early Star Formation. *Phys. Rev. Lett.* **2017**, *119*, 041102.

38. Ivanov, P. Nonlinear Metric Perturbations and Production of Primordial Black Holes. *Phys. Rev. D* **1994**, *50*, 7173–7178.

39. Ashoorioon, A.; Dimopoulos, K.; Sheikh-Jabbari, M. M.; Shiu, G. Non-Gaussianities in Bouncing Cosmologies and Primordial Black Holes. *Phys. Rev. D* **2019**, *100*, 103532.

40. Lesgourgues, J. The Cosmic Linear Anisotropy Solving System (CLASS) I: Overview. *arXiv* **2011**, arXiv:1104.2932.

41. Lewis, A.; Challinor, A. Efficient Computation of CMB Anisotropies in Closed FRW Models. *Astrophys. J.* **2000**, *538*, 473–476.

42. Springel, V. GADGET-4: A Novel Code for Collisionless Simulations of Structure Formation. *Mon. Not. R. Astron. Soc.* **2021**, *506*, 2871–2949.

43. Penrose, R. Cycles of Time: An Extraordinary New View of the Universe. *Bodley Head* **2010**.

44. Bekenstein, J. D. Black Holes and Entropy. *Phys. Rev. D* **1973**, *7*, 2333–2346.

45. Susskind, L. The World as a Hologram. *J. Math. Phys.* **1995**, *36*, 6377–6396.

46. t Hooft, G. Dimensional Reduction in Quantum Gravity. *In* Salam Festschrift; World Scientific: Singapore, 1993.

47. Bousso, R. The Holographic Principle. *Rev. Mod. Phys.* **2002**, *74*, 825–874.

48. Landauer, R. Irreversibility and Heat Generation in the Computing Process. *IBM J. Res. Dev.* **1961**, *5*, 183–191.

49. Neukart, F. The Quantum Memory Matrix: Discrete Spacetime as an Information Ledger. *Ann. Phys.* **2024**, *456*, 168944.

50. Neukart, F. Gravity–Information Duality: Quantum Entanglement Contributions to Gravitational Dynamics. *Ann. Phys.* **2025**, *463*, 169032.

51. Ashtekar, A.; Pawlowski, T.; Singh, P. Quantum Nature of the Big Bang: Improved Dynamics. *Phys. Rev. D* **2006**, *74*, 084003.

52. Valageas, P.; Schaeffer, R.; Silk, J. Entropy of the Intergalactic Medium and Massive Galaxy Formation. *Astron. Astrophys.* **2002**, *388*, 741–757.

53. Shankar, F.; Bernardi, M.; Sheth, R. K. Selection Bias in Dynamically Measured Super-Massive Black Hole Scaling Relations. *Mon. Not. R. Astron. Soc.* **2016**, *460*, 3119–3142.

54. Inayoshi, K.; Visbal, E.; Haiman, Z. The Assembly of the First Massive Black Holes. *Ann. Rev. Astron. Astrophys.* **2020**, *58*, 27–97.

55. Egan, C. A.; Lineweaver, C. H. A Larger Estimate of the Entropy of the Universe. *Astrophys. J.* **2010**, *710*, 1825–1834.

56. Moresco, M.; Pozzetti, L.; Cimatti, A.; *et al.* A 6% Measurement of the Hubble Parameter at $z \approx 0.45$: Direct Evidence of the Epoch of Cosmic Re-acceleration. *J. Cosmol. Astropart. Phys.* **2016**, *05*, 014.

57. Riess, A. G.; Casertano, S.; Yuan, W.; *et al.* Cosmic Distances Calibrated to 1% Precision with *Gaia* EDR3 Parallaxes and *Hubble Space Telescope* Photometry of 75 Milky Way Cepheids. *Astrophys. J. Lett.* **2021**, *908*, L6.

58. Alam, S.; Aubert, M.; Avila, S.; *et al.* Completed SDSS-IV eBOSS: Cosmological Implications from Two Decades of Spectroscopic Surveys at the Apache Point Observatory. *Phys. Rev. D* **2021**, *103*, 083533.

59. Pitrou, C.; Coc, A.; Uzan, J. P.; Vangioni, E. Precision Big-Bang Nucleosynthesis with Improved Helium-4 Predictions. *Phys. Rept.* **2018**, *754*, 1–66.

60. DES Collaboration. Dark Energy Survey Year 3 Results: Cosmological Constraints from Galaxy Clustering and Weak Lensing. *Phys. Rev. D* **2022**, *105*, 023520.

61. Misner, C. W.; Sharp, D. H. Relativistic Equations for Adiabatic, Spherically Symmetric Gravitational Collapse. *Phys. Rev.* **1964**, *136*, B571–B576.

62. Kodama, H. Conserved Energy Flux for the Spherically Symmetric System and the Back Reaction Problem in the Black Hole Evaporation. *Prog. Theor. Phys.* **1980**, *63*, 1217–1228.

63. Planck Collaboration. Planck 2018 Results. VI. Cosmological Parameters. *Astron. Astrophys.* **2020**, *641*, A6.

64. Caldwell, R. R.; Kamionkowski, M.; Weinberg, N. N. Phantom Energy and Cosmic Doomsday. *Phys. Rev. Lett.* **2003**, *91*, 071301.

65. Lehners, J. L. Ekpyrotic and Cyclic Cosmology. *Phys. Rept.* **2008**, *465*, 223–263.

66. Biswas, T.; Mazumdar, A.; Shafieloo, A. Cyclic Inflation. *Phys. Rev. D* **2010**, *82*, 123517.

67. Bertone, G.; Hooper, D. History of Dark Matter. *Rev. Mod. Phys.* **2018**, *90*, 045002.

68. Carr, B.; Kohri, K.; Sendouda, Y.; Yokoyama, J. Constraints on Primordial Black Holes. *Rep. Prog. Phys.* **2020**, *84*, 116902.

69. Amaro-Seoane, P.; Audley, H.; Babak, S.; *et al.* Laser Interferometer Space Antenna. *arXiv* **2017**, arXiv:1702.00786.

70. Bouwens, R. J.; Illingworth, G. D.; Stefanon, M.; *et al.* Early Results from GLASS-JWST: Galaxy Candidates at $z \gtrsim 13$. *Astrophys. J. Lett.* **2022**, *931*, L20.

71. Israel, W. Singular Hypersurfaces and Thin Shells in General Relativity. *Nuovo Cim. B* **1966**, *44*, 1–14.

72. Vassilevich, D. V. Heat Kernel Expansion: User's Manual. *Phys. Rept.* **2003**, *388*, 279–360.

73. Parker, L.; Toms, D. J. *Quantum Field Theory in Curved Spacetime*; Cambridge University Press: Cambridge, UK, 2009.

74. Dormand, J. R.; Prince, P. J. A Family of Embedded Runge–Kutta Formulae. *J. Comput. Appl. Math.* **1980**, *6*, 19–26.